International Journal of Hydrogen Energy 67 (2024) 1248–1261

Contents lists available atScienceDirect

International Journal of Hydrogen Energy

journal homepage: www.elsevier.com/locate/he

Fischer-tropsch synthesis of fuels and olefins in 3D printed SS microreactor using iron/graphene oxide catalysts with Mn- and Na-metal promoters

Saif Hassan [a], Meric Arslan [b], Juvairia Shajahan [c], Sujoy Bepari [a], Punprabhashi Vidanapathirana [b], Debasish Kuila [a,b,*]

[a] Department of Chemistry, North Carolina Agricultural and Technical State University, Greensboro, NC, 27411, United States

[b] Department of Applied Science and Technology, North Carolina Agricultural and Technical State University, Greensboro, NC, 27411, United States [c] Joint School of Nanoscience and Nanoengineering, North Carolina Agricultural and Technical State University, Greensboro, NC, 27411, United States

ARTICLEINFO

Handling Editor: Arunachala Kannan

Keywords:
FT synthesis
SS microreactor Fe catalyst
Graphene oxide
Carbon-based catalyst support

ABSTRACT

The effects of adding Mn and Na promoter metals to graphene oxide (GO)-supported iron-based catalysts for Ficher-Tropsch Synthesis (FTS) reactions to olefins at 20 bars were investigated in a 3D-printed stainless steel (SS) Microreactor. While promoter metals encourage reduction of iron oxide to iron to form iron carbide, the active metal catalysts in GO allow hydrogenation of CO. These catalysts were synthesized by layer deposition method and characterized by different techniques. The TEM images show the integration of graphene oxide into the catalysts. The XRD and XPS studies confirmed the crystal structure and oxidation states of the metals. The catalytic activity and product selectivity were studied in the temperature range of 200–350°Cwith a 2:1 M ratio of H_2: CO. Higher CO conversion with greater selectivity for olefins was observed in the presence of the promoters. FeMnNa@GO showed better stability than both Fe@GO and FeMn@GO catalysts in time-on-stream studies.

1. Introduction

Fischer-Tropsch synthesis (FTS) is a specialized reaction in which carbon monoxide (CO) and hydrogen (H_2) react to form hydrocarbons in the presence of heterogeneous Fe-based catalysts [1]. Syngas (Sythesis gas), composed of CO and H_2, can be produced via a wide range of reforming processes from biomass gasification. Agricultural byproducts, such as lumber and animal waste are treated to produce syngas, which in turn is converted to hydrocarbons via FTS [2–10]. While the exact mechanism of FTS is not yet known, the active metal catalysts provide hydrogenation of CO to form "CH_2" which undergo C–C coupling or further hydrogenation [11,12]. One of the challenges in FTS is the high temperature required to complete the reaction and the high selectivity for CH_4 and CO_2 as undesirable products [13,14]. CO conversion measures the efficiency of the catalyst in hydrogenation of CO. However, product selectivity is important for the viability of the process [14,15]. Extensive efforts have been made to overcome the apparent trade-off between olefin selectivity and CO conversion using FTS catalysts [14]. Olefins are useful byproducts that can be used to build recycled plastic materials, such as polyethylene and polypropylene [16].

For FTS reactions, some of the developed catalysts include Fe@CNFs (carbon nanofibers), Fe@Al_2O_3, and $ZnCrO_x$@SAPO-34 with Na and S promoters [17–19]. Metals such as Fe, Ru, and Co are the most widely used materials for FTS [20,21]. Iron-based catalysts have proven to be efficient and cost-effective for FTO synthesis due to the fact that iron discourages the competing water-gas shift reaction [17]. Therefore, Fe-based catalysts were investigated in this study. To facilitate further C–C coupling to form C_2–C_4 olefins or biofuels, carbon-based support such as graphene oxide was considered in this work. Graphene oxide has shown excellent product selectivity towards long-chain carbons and low selectivity towards CO_2 and CH_4 [22]. In addition, it has higher selectivity to olefins [23,24]. There are some research works reported on graphene oxide supporting Fe and Co based catalysts for Fischer-Tropsch synthesis (FTS). Moussa et al. [25] studied the graphene oxide supported Fe–K catalysts for FTS process. They found that graphene oxide reduced the water-gas shift (WGS) reaction activity compared to carbon nanotubes (CNTs). As a result, the formation of CO_2 is significantly reduced. The catalysts showed high activity and selectivity due to the presence of defects within the graphene lattice that acts as nucleation sites for metal nanoparticles, providing tunable metal-support interactions. Cheng et al. [26] reported FTS to lower olefins by FeK on reduced graphene oxide (rGO) catalysts. In the presence of K, the lower olefins selectivity increased up to 68% and olefin/paraffin ratio of 1:1 in the C_2–C_4 hydrocarbons. Similar kinds of study related with hierarchically mesoporous iron oxide/graphene oxide (GO) composites have been synthesized for FTS process by Wei et al. [27]. The catalysts exhibited higher surface area, higher porosity, and weaker Fe-GO interaction. The weaker interaction between Fe-GO helped to reduce the catalyst at lower temperature. The hierarchical pore structure increases the number of active sites and promotes the mass transfer of reactants and products. The Fe-based GO supported catalyst with glucose was synthesized by Wei et al. [28]. They observed that the addition of glucose can generate spatial confinement between GO sheets, which helped to grow iron oxide nanoparticles and tune the particle size. Cheng et al. [29] reported Fe-based Mg and K metals catalysts with GO support for lower olefins production. They showed that the addition of Mg and K metals enhanced the olefin selectivity as well as the reduction of CO_2 formation during FTS. The nitrogen

* Corresponding author. Department of Chemistry, North Carolina Agricultural and Technical State University, Greensboro, NC, 27411, United States. *E-mail address:* dkuila@ncat.edu (D. Kuila).

https://doi.org/10.1016/j.ijhydene.2024.03.086

Received 22 November 2023; Received in revised form 1 March 2024; Accepted 6 March 2024 Available online 23 March 2024

functionalized GO supported Co and Ru metals catalysts were prepared for FTS process by Taghavi et al. [30]. They reported that the functionalization with N_2 helped to reduce the catalyst at lower temperature and increase the Co particles dispersion and CO conversion from 70.6 to 74.5%.

This paper attempts to expand the studies on carbon nano-fiber support catalysts in the form of graphene oxide nanosheets to aid iron- based catalysts. Graphene oxide is a single-layered honeycomb structured material. It is composed of sp^2 hybridized carbon atom. It can be potentially used in energy storage, electronics and other areas due to its special monoatomic layered structure, superior mechanical, thermal, electrochemical and optical properties [31]. This material has superior specific surface area, thermal conductivity, chemical stability and mechanical strength. So, it can be used as catalyst support. The unique microstructure of this material is suitable for heterogeneous catalytic applications [32]. The promising carbon-based materials (graphene oxide) exhibit weak metal-support interaction, which accelerates active metal and promoter's reduction and increases the catalytic activity [33].

The geometry of the support also has a major impact on the activity of the catalyst. Recently, the synthesis of catalysts with core-shell geometries has been emphasized, where the support acts as a shell and surrounds the active metal nanoparticle cores. This structure is advantageous because the pores in the supports confine reactants to the active metal, and the shell also serves to protect the active metal and its active sites from degradation. These two factors have been shown to enhance both the conversion and selectivity of FTS reactions [34,35]. Furthermore, promoter metals are used to encourage the catalyst to be reduced at lower temperatures by providing electrons to maintain Fe in its active state, Fe^0, which encourages olefin production over single-carbon gas (CH_4 and CO_2) production [36]. In this study, manganese and sodium were used in conjunction with iron and supported by graphene oxide for FTO sy nthesis. The loadings of these promoter metals in the catalysts were varied, and their effects on catalyst characteristics and activity, as well as product selectivity, were investigated. The
Anderson-Schulz-Flory (ASF) model explains the product selectivity of FTS reactions, asserting that the product molecular weight distribution is determined by the chain growth probability factor α. A high value of factor α (>0.90) correlates with high selectivity towards heavy hydrocarbons, which could include olefins and liquid fuels [11,37].

2. Experimental section

2.1. Materials

The reagents $FeCl_3{\cdot}6H_2O$, $MnSO_4$, Na_2CO_3, NaOH, Ethanol (anhydrous), N, *N*-dimethylformamide (99%), Graphene Oxide powder, concentrated sulfuric acid, and concentrated nitric acid were procured from Sigma Aldrich. Analytical-grade solvents and reagents were utilized without additional purification.

2.2. Catalyst preparation

Three GO-supported metal catalysts were synthesized using the layer deposition method described below: Fe@GO, FeMn@GO, and FeMnNa@GO.

2.2.1. Preparation of FeMnNa cores

FeMnNa cores were prepared by layer-by-layer deposition as described elsewhere [38]. Fe^{3+} and Mn^{2+} solutions (20 ml) prepared using $FeCl_3$ and $MnSO_4$ were added to 40 ml of EtOH such that the molar ratio of Fe_3O_4:MnO_2 in the core was 8:1 or 1:1. The metal hydroxides were precipitated by the dropwise addition of NH_4OH until the pH of the solution was 9. The obtained slurry was irradiated in a microwave oven at 180 W for 30s (10s on and 20s off) for 10min. The collected precipitate was washed with distilled water and ethanol (1:1 ratio), dried at 100 °C for 1 h, and then calcined at 500 °C for 2 h. This produced the

Fe_3O_4/MnO_2 core.

In order to have Na-oxide at the core, Na_2CO_3 was dispersed in 50 ml EtOH such that the molar ratio of Fe_3O_4:MnO_2:Na_2O in the core was 1:1:1 or 8:1:1. Fe_3O_4@MnO_2 powder was gradually added to the dispersion under constant dynamic stirring. EtOH was evaporated to obtain a solid, which was then dried at 110 °C for 12 h and calcined at 500 °C for 4 h to prepare FeMnNa(x:1:1), where x was either 8 or 1 based on the molar ratio of Fe_3O_4:MnO_2:Na_2O in the core. *2.2.2. Preparation of FeMnNa(x:1:1)@GO (graphene oxide nanosheets)*

2.2.2.1. Preparation of GO nanosheets. Aqueous graphene oxide (GO; 120 ml, 5 mg/ml) was treated with 32 ml of concentrated nitric acid and 8 ml of concentrated sulfuric acid at 80 °C for 24 h in order to cut the sheets into nanosheets [39,40]. Subsequently, the solution at room temperature was dispersed for 30 min and neutralized to pH 7.0 with NaOH and filtered using 44-μm filters.

2.2.2.2. Attaching GO shell to metal oxide cores. GO (0.2 g) was dispersed in dimethylformamide (DMF) using an ultrasonicator and stirred vigorously for 2 h. Then, 1 g of the metal-oxide core was dispersed by stirring for 24 h. The precipitate was isolated by centrifugation, thoroughly washed with ethanol and water, and dried overnight at 100 °C. The FeMnNa@GO catalyst was calcined under Ar at 500 °C for 6 h.

2.3. Catalyst characterization A physisorption analyzer (3Flex, Micromeritics, USA) was used for the Brunauer-Emmett-Teller (BET) surface area measurements and N_2 isotherms of the catalysts. The Barrett-Joyner-Halenda (BJH) technique was employed to get the pore sizes and their distributions. The same Micromerictics instrument in the dynamic analysis mode was used for temperature programmed reduction (TPR) studies with 10% H_2 (v/v) (rest Ar gas) in the temperature range of room temperature to 1000 °C. The scanning Electron Microscopy (SEM) studies of the catalysts were performed using ZEISS Auriga Focused Ion Beam Scanning Electron Microscope (FIBSEM), while Transmission Electron Microscopy (TEM) of materials using Thermo Fischer Talos (Model: F200X) instrument where the field emission system was kept at a voltage of 200 kV at JSNN. Thermal degradation of the catalysts and the deactivated (spent) catalysts was performed using Thermogravimetric Analysis and Differential Scanning Calorimetry (TGA-DSC) (Model: TA Instruments, New Castle, DE, USA). The fresh and spent catalysts were heated to 1000 °C at a rate of 10 °C/min under N_2 or Air flow of 40 mL/min. X-ray photoelectron spectroscopy (XPS) (Model: Escalab Xi + -, Make: Thermo Scientific, West Sussex, UK) was used to identify the oxidation states of all catalysts. X-ray diffraction (Model: Rikagu) analysis was carried out using a diffractometer (Model: Rikagu) with a detection limit between 10 and 80° with a step size of 0.02° and a Cu K1 radiation with wavelength of 1.5406 Å.

2.4. Catalyst activity test

The FTS reactions were performed in a microfluidic 3-D printed SS reactor using a setup built in our laboratory with LabVIEW programming to control the temperature of the reactions and gas flow rates. The reactor comprises of seven microchannels measuring 1000μmx1000mx5cms (Fig. S1) [32]. Two mass flow controllers (Bronkhorst) were employed to maintain the (H_2 and CO in a 2:1 ratio) flow of the syngas mixture. A mass flow controller (Aalborg) was used to control the N_2 flow. Bronkhorst pressure gauges monitored the pressure and communicated with an Aalborg back-pressure controller, which controlled the reaction pressure. The gaseous products were identified using Gas Chromatography (Agilent 7890 B GC) with a mass selective detector (Agilent 5977 MSD). The reduction of the catalysts, prior to the reactions was done overnight in the microreactor at 350 °C. The gas hourly space velocity (GHSV) of the Fischer-Tropsch reaction was maintained at 12000 h^{-1}. While the flow rate for N_2 was 1.5 ml/min, for H_2 and CO they were 4 ml/min and 2 ml/min, respectively. All the catalytic reactions were carried out at 20 bars.

2.5. Catalyst characterization

2.5.1. BET analysis

The N_2 adsorption/desorption isotherms of all the catalysts (Fig. 1a) showed a type IV isotherm with an H3 hysteresis loop [41]. This result indicates that the mesoporous and microporous structures had many gaps. The pore-size distribution (PSD) of all catalysts are shown in Fig. 1b. The maximum number of pores was observed in the range of 3–20 nm. The spaces between the aggregated catalyst nanoparticles may be responsible for these mesopores [42].

The surface properties of all the catalysts are shown in Table 1. The surface area of the Fe@GO catalyst, 60.59 m^2/g, decreases to 50.38 m^2/ g for the FeMn@GO catalyst. It further decreases to 47.01 m^2/g for the FeMnNa@GO catalyst. The declining trend in the surface area corresponds to the combined addition of Mn and Na. Further, the addition of Na affected the interaction between Mn and Fe, resulting in the lowest surface area [43]. In the case of the FeMn@GO catalyst, the mesopore pore volume and pore diameter decreased owing to the addition of Mn

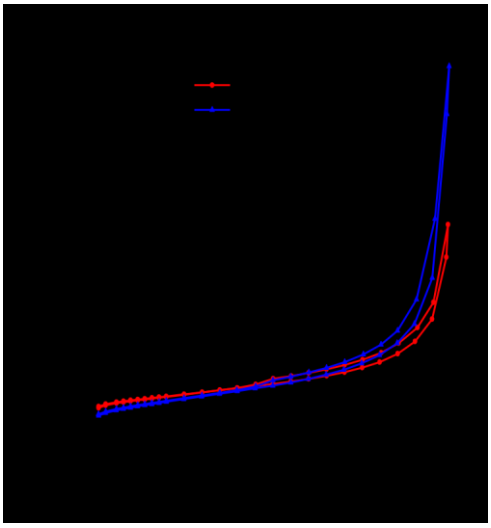

Table 1
BET surface areas, pore volumes, and pore diameters of different catalysts.

Catalyst	Sp. Surface area (m^2/ g)	Pore Volume (cc/ g)	Pore diameter (nm)
Fe@GO	60.59	0.25	16.55
FeMn@GO	50.38	0.14	10.79
FeMnNa@GO	47.01	0.23	19.76

nanoparticles. This change was assigned to the reduction of mesopores formed by the aggregation of FeMn nanoparticles. The decrease of pore volume with increase in the pore diameter is observed for the FeMnNa@GO catalyst.

2.5.2. TEM analysis

Fig. 2 shows the TEM images of the Fe@GO, FeMn@GO, and FeMnNa@GO catalysts. The particle size was determined using ImageJ software for all the catalysts. The sheet-like morphology of typical graphene oxide was observed in the catalyst images [24]. In the case of the Fe@GO catalyst, Fe_3O_4 nanoparticles were distributed over a graphene oxide sheet (Fig. 2a). The Fe_3O_4 nanoparticles were 20.81 nm. The nanoparticles of the FeMn@GO catalyst were larger than those of the Fe@GO catalyst. The average FeMn@GO particle size is 65.38 nm. The TEM image of the FeMn@GO catalyst suggests that the particle size increases upon addition of Mn (Fig. 2b). This is due to the agglomeration of nanoparticles of Mn and Fe_3O_4 [44]. The nanoparticle size decreased with the addition of Na for the FeMnNa@GO catalyst. The nanoparticle size is 30.72 nm for the FeMnNa@GO catalyst. The TEM image clearly shows that the particle size decreased (Fig. 2c). So, the addition of Na affects the interaction of Mn with Fe_3O_4 nanoparticles. TEM analysis can be correlated with the BET studies.

2.5.3. SEM-EDS analysis

The morphologies and structures of the Fe@GO, FeMn@GO, and FeMnNa@GO catalysts were revealed by SEM analysis. Fig. 3 shows the SEM images of all catalysts. The SEM image depicts large Fe_3O_4 nanoparticles with a typical particle size of 240.68 nm (Fig. 3a). It shows the agglomeration of Fe_3O_4 nanoparticles, yielding a large particle size [45], which indicates a low surface area and pore volume (BET analysis) [46]. The relatively smaller particle size was determined using ImageJ software for the FeMn@GO and FeMnNa@GO catalysts. The particle sizes

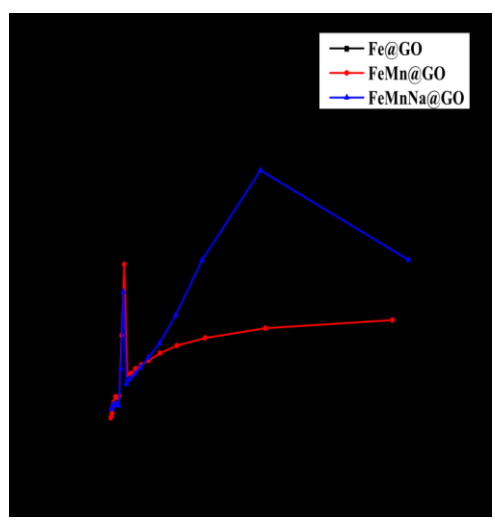

Fig. 1. BET analyses of all catalysts: (a) Isotherm plot; (b) Pore-size distribution (PSD) plot.

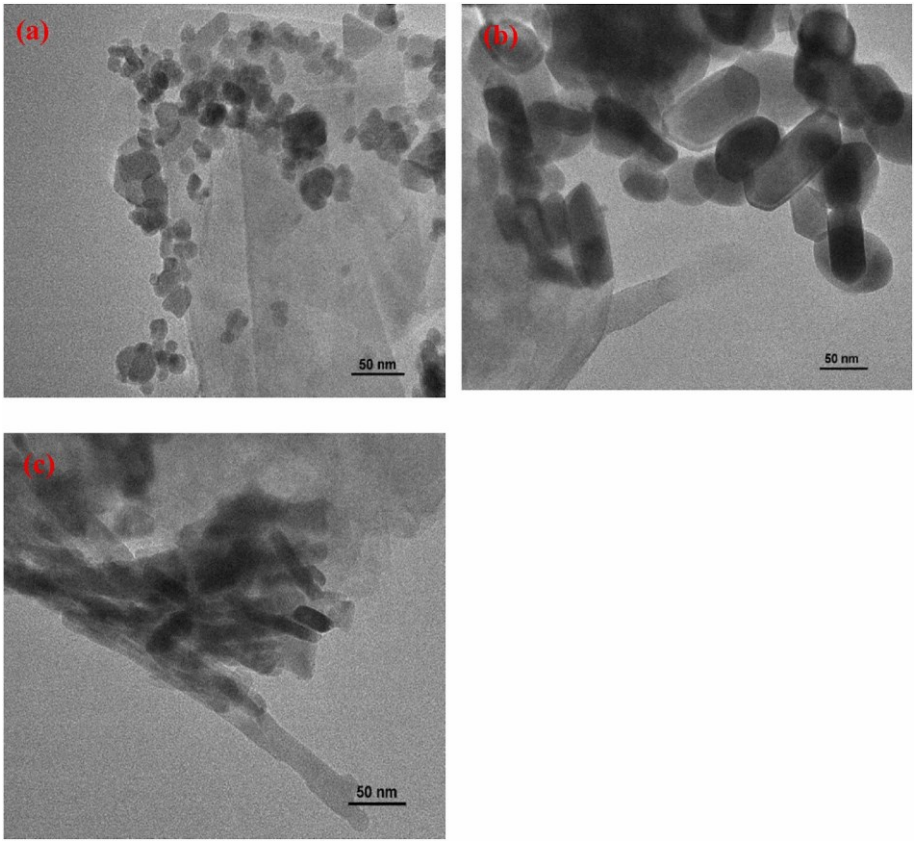

Fig. 2. TEM images of (a) Fe@GO, (b) FeMn@GO, and (c) FeMnNa@GO catalysts.

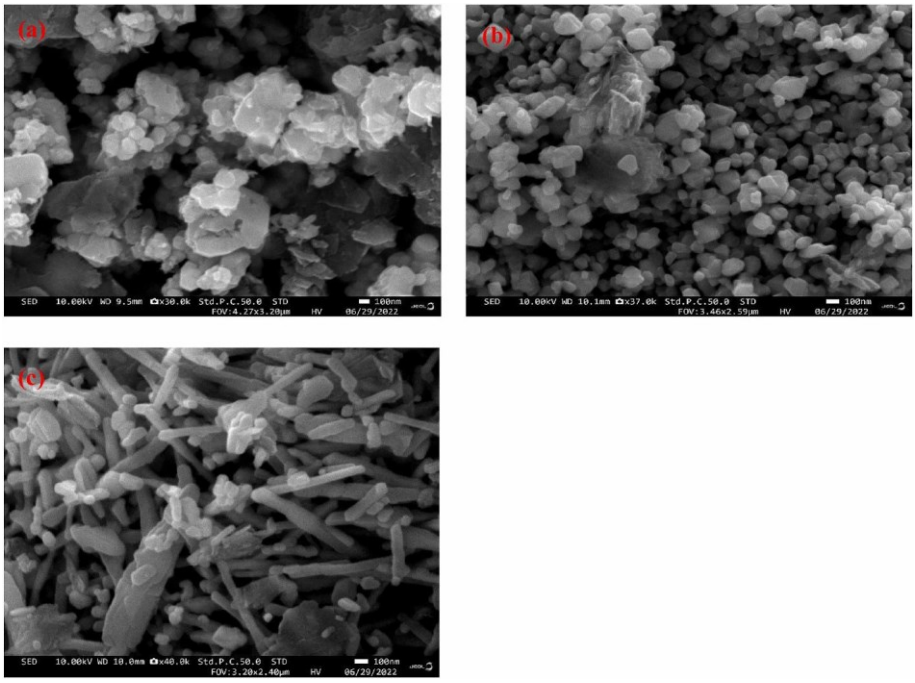

Fig. 3. SEM images of (a) Fe@GO, (b) FeMn@GO, and (c) FeMnNa@GO catalysts.

are 194.24 nm (FeMn@GO) and 162.43 nm (FeMnNa@GO) respectively. Incorporation of Mn and Na into the catalysts is the main reason for the reduction in particle size. The SEM images (Fig. 3b and c) suggest that the formation of small particles was due to the addition of Mn and Na. A rod-like structure was observed in the FeMnNa@GO catalyst (Fig. 3c). This structure may be formed due to the interaction of metals (Fe, Mn, and Na) with the graphene oxide nanosheets.

Table 2 depicts the energy-dispersive X-ray spectroscopy (EDS) results. The Fe@GO catalyst mainly contained Fe, C, and O atoms. The presence of C was attributed to the graphene oxide sheet. These elements

Table 2
EDS analyses of all catalysts.

Catalyst	Metal wt.%				
	Fe	Mn	Na	C	O
Fe@GO	66.68	–	16.74	16.58	–
FeMn@GO	53.6	2.52	–	19.47	24.41
FeMnNa@GO	48.09	2.35	1.54	20.14	27.87

were well distributed in the Fe@GO catalyst. The metal loading of the FeMn@GO and FeMnNa@GO catalysts was altered by the incorporation of Mn and Na. In the EDS analysis, the presence of oxygen was attributed to metal oxidation on the catalyst surface.

2.5.4. TPR analysis

Fig. 4 demonstrates the H_2-TPR analysis and the reduction behavior of the Fe@GO, FeMn@GO, and FeMnNa@GO catalysts. Two reduction peaks were observed for the Fe@GO catalyst at 600 °C and 819 °C (Fig. 4a). The peak at 600 °C, which is within the range of 500–730 °C, is allocated to the continuous reduction of Fe_3O_4 to FeO and FeO to metallic Fe [46]. In the presence of GO, this reduction process is suppressed due to the interactions, which occurred between the O_2-holding groups in GO and Fe species [23]. The reduction peak at approximately 819 °C corresponds to gasification of the GO support. In this process, oxygen-containing groups, such as carboxylic groups, present in GO can be reduced with hydrogen to release CO [47,48]. In the case of the FeMn@GO catalyst (Fig. 4b), the peak at 490 °C was split into three peaks upon the addition of Mn. The peak at 418 °C corresponds to the reduction of MnO_x containing Fe_3O_4($Fe_xMn_{3-x}O_4$) to manganowusite ($Fe_xMn_{1-x}O$), which is accompanied by a lower reduction temperature [49]. The peaks at approximately 530 °C and 588 °C are due to the reduction of manganowusite to metallic Fe and MnO [50]. The addition of Na to the FeMnNa@GO catalyst caused a slight shift in the reduction peak to a lower temperature (Fig. 4c). This result can be ascribed to the strong interaction between Fe and Mn, which is evident from TEM studies. Moreover, the incorporation of the alkali metal Na enhanced the reduction of the Fe–Mn catalyst in the H_2 environment because of its basicity and the donation of electrons from Na [51]. The three peaks (at 400, 548, and 674 °C) can be allocated to the reduction of MnO_x containing Fe_3O_4($Fe_xMn_{3-x}O_4$) to manganowusite ($Fe_xMn_{1-x}O$) and manganowusite to metallic Fe and MnO.

The H_2 consumption studies for the three different catalysts are illustrated in Table 3. The highest H_2 consumption was observed for the Fe@GO catalyst. The FeMn@GO catalyst exhibited the lowest H_2

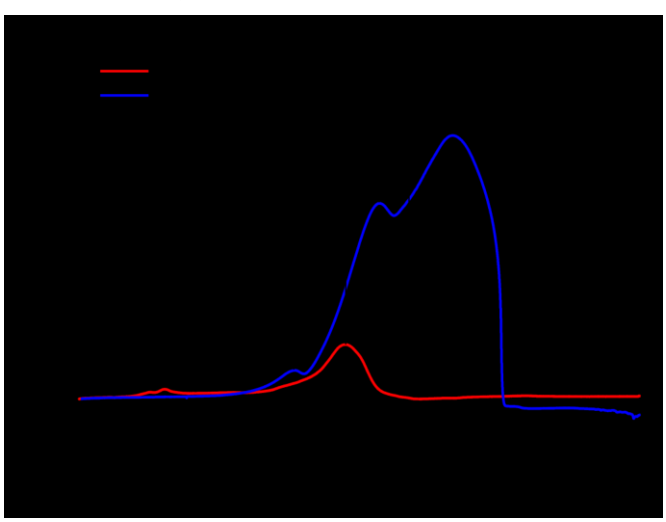

Fig. 4. H_2-TPR analysis of (a) Fe@GO; (b) FeMn@GO; (c) FeMnNa@GO catalysts.

Table 3
H_2 consumption of different catalysts in H_2-TPR analysis.

Catalyst	H_2 Consumption (mmol/g)
Fe@GO	4.26
FeMn@GO	0.40
FeMnNa@GO	3.68

consumption. This result suggests that the Fe–Mn interaction causes the entry of Mn into the Fe_3O_4 lattice, which inhibits H_2 consumption during TPR analysis [52].

2.5.5. XRD analysis

XRD analysis was carried out to identify the different phases of the metal oxides, as showed in Fig. 5. The fresh Fe@GO catalyst exhibited diffraction peaks at 2θ values of 30.04°(220), 35.43°(311), 43.09° (400),53.82°(422),56.96°(333), and 62.54°(440), which correspond to the cubic structure of the Fe_3O_4 phase (JCPDS 79–0417) (Fig. 5a) [41]. In the case of the FeMn@GO and FeMnNa@GO catalysts (Fig. 5 (b) and (c)), the cubic structure of Mn_2O_3 was formed along with the Fe_3O_4 phase. The Mn_2O_3 (JCPDS 78–0390) diffraction peaks are observed at 2θ value of 24°(211), 26.36°(220), 32.9°(222), 40.51°(411), 49.2°(134), 63.89°(145), 72°(046) and 75.45°(642). However, no characteristic peaks of Na were observed, possibly because of its good dispersion in the
Fe_3O_4 phase [53].

The crystal sizes calculated from the XRD data are listed in Table 4. The typical crystal sizes of the Fe_3O_4 and Mn_2O_3 phases were determined using the modified Scherrer equation [54]. The Fe_3O_4 crystal size in the Fe@GO catalyst was 20.04 nm, almost the same as that obtained in the TEM analysis. The Fe_3O_4 and Mn_2O_3 crystal sizes are 30.61 and 31.19 nm for FeMn@GO, respectively. The crystal size increased upon addition of Mn nanoparticles. The crystal sizes can also be correlated with TEM analysis. The crystal sizes of Fe_3O_4 and Mn_2O_3 nanoparticles

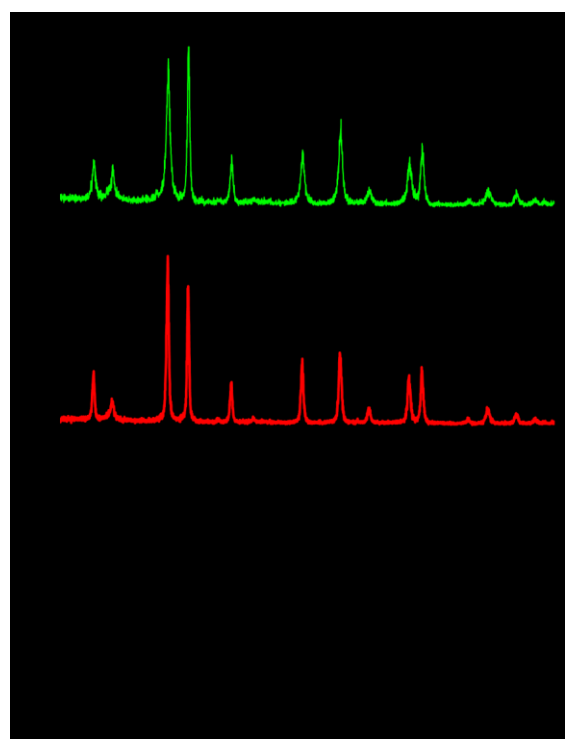

Fig. 5. XRD patterns of (a) Fe@GO; (b) FeMn@GO; (c) FeMnNa@GO catalysts.

Table 4
Crystal sizes[a] based on XRD analysis.

Catalyst	Avg. crystal size (nm) (Fe_3O_4)	Avg. crystal size (nm) (Mn_2O_3)
Fe@GO	20.04	–
FeMn@GO	30.61	31.19

FeMnNa@GO	17.46	25.05

[a] The modified Scherrer equation was used to calculate size [54]. are 17.46

and 25.05 nm for the FeMnNa@GO catalyst.

2.5.6. TGA-DSC (AS) analysis

TGA measures the weight loss of the catalyst and provides the degradation temperature. DSC analysis shows the heat flow in and out of the sample and is set to "exothermic up," meaning that a local minimum in the curve represents an endothermic process, such as melting or evaporation, and a local maximum represents an exothermic process, such as crystallization [55–58]. The heat flow and weight loss of the catalysts as functions of temperature are shown below (Fig. 6). The TGA-DSC analysis shows the temperatures at which templating or structuring agents can be removed from the catalyst.

The unpromoted Fe@GO catalyst (As = as such) displayed steady weight loss from 200 to 800 °C, followed by a high rate of weight loss at 800 °C. At the end of the analysis, the catalyst weighed approximately 60% of its initial weight. The heat flow curve showed an endothermic peak at approximately 800 °C, corresponding to precipitous weight loss, and underwent thermal degradation at 800 °C [55]. However, both the promoted catalysts retained approximately 90% of their original weight until the analysis reached 800 °C. This suggests that the promoted catalysts were more stable at temperatures up to 800 °C and may be more stable at higher temperatures or for longer use in time-on-stream studies.

2.5.7. XPS analysis

X-ray Photoelectron Spectroscopy (XPS) offered valuable insights into the bonding characteristics and oxidation states of the metal. The deconvoluted XPS spectra of the C1s scan were used for charge correction with the binding energy of C–C at 284.8 eV. This correction ensured precise charge adjustments for all elemental spectra, facilitating a more accurate analysis of the bonding and oxidation of the catalyst.

In the C1s spectrum (Fig. 7a) of the catalyst, Fe@GO exhibits a complex spectrum due to the presence of Fe. The splitting of sp^3 and sp^2 hybridization of C–C can be observed with a difference of 1.5eV at 284.75 eV and 283.25 eV [59], confirming the presence of graphene oxide. The TEM imaging further confirmed graphene oxide in the samples. In the C1s Spectra of the Fe@GO catalyst, the O–C̅–O peak is visible at 288.90 eV and the C–*O*–C peak is observed at 285.76 eV [59].

In the O1s spectrum (Fig. 7b) of the catalyst Fe@GO, there are 3 major peaks denoting the presence of organic C–O, metal oxides, and metal carbonates at 531.59eV, 529.98 eV, 530.80 eV, respectively [60]. Metal carbonates could forme by the interaction of the precursor material with Fe [60].

The Fe2p spectrum (Fig. 7c) of the Fe@GO catalyst confirms the formation of Fe_3O_4, which is consistent with the XRD results. The deconvolution of the Fe2p spectrum has the satellite peaks of $Fe2p_{1/2}$ and $Fe2p_{3/2}$ at 732.45eV and 718.27eV binding energies [61]. The Fe^{3+} oxidation peak at 727.44eV and Fe^{2+} oxidation peak at 723.91eV can be observed within the deconvoluted peak of $Fe2p_{1/2}$. And Fe^{3+} oxidation peak at 712.39eV [62] and Fe^{2+} oxidation peak at 709.90eV can also be observed within the deconvoluted peak of $Fe2p_{3/2}$ [61]

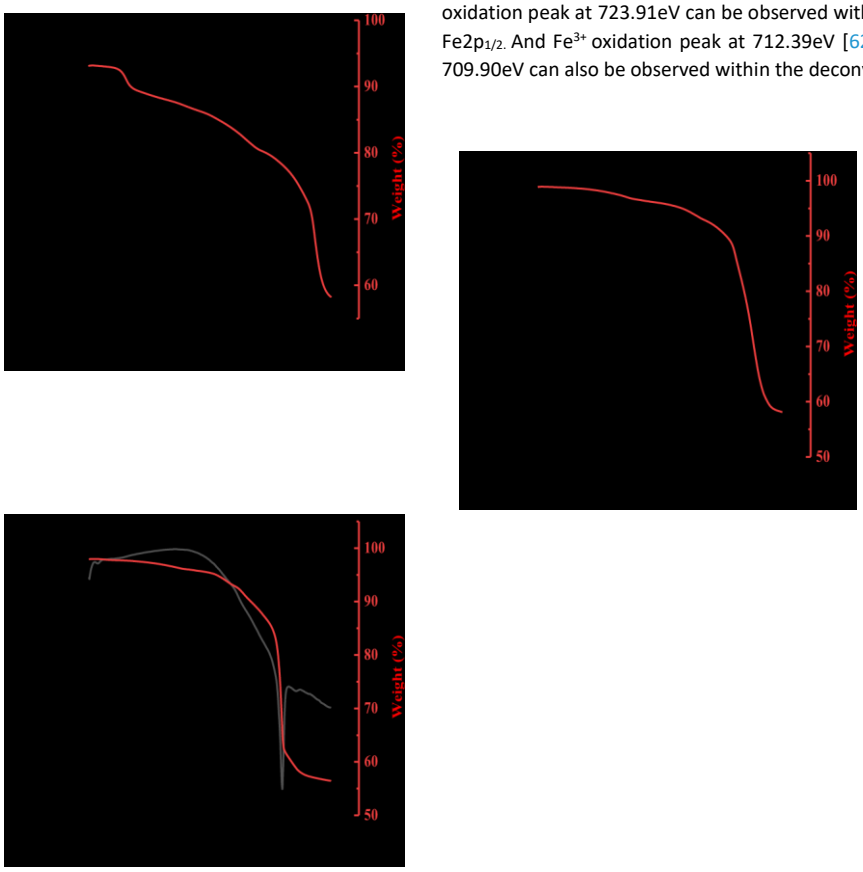

Fig. 6. TGA-DSC profiles of (a) Fe@GO (As); (b) FeMn@GO (As); (c) FeMnNa@GO (As) catalysts.

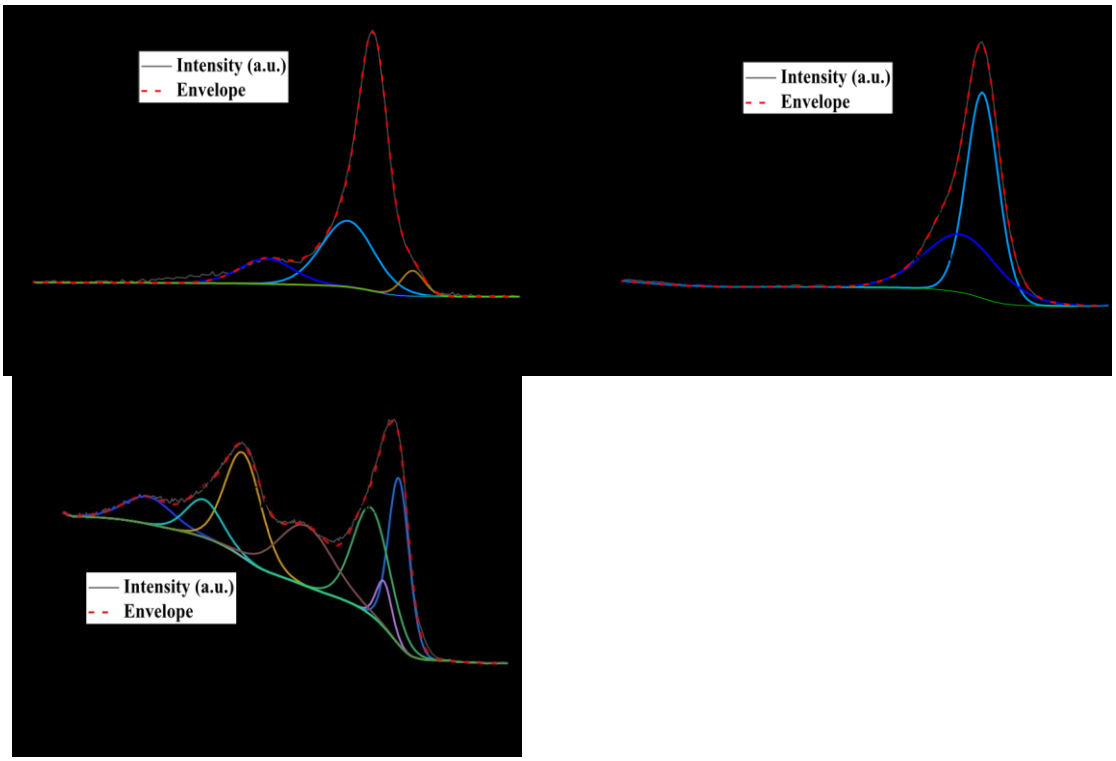

Fig. 7. XPS analyses of (a) C1s; (b) O1s; (c) Fe2p for Fe@GO catalyst.

Due to the presence of metals, the C1s of XPS spectrum of FeMn@GO exhibits a complex spectrum [50]. In the C1s spectrum (Fig. 8a) of the catalyst FeMn@GO, the peaks of C–C, C–O, and O–C¯–O are detected at 284.78eV, 286.71eV, and 288.58eV, respectively [59].

In the O1s spectrum (Fig. 8b) of FeMn@GO, there are three major peaks denoting the presence of Organic C–O, Organic C¯–O, and metal oxides at 531.44eV, 533.26 eV, 529.80 eV, respectively [60]. The Na auger peak is visible in the O1s spectrum at 535.26 eV due to the residues from the precursor materials.

The Fe2p spectrum (Fig. 8c) acquired from the FeMn@GO catalyst provides compelling evidence for the formation of Fe_3O_4 [63], which is consistent with the findings from X-ray Diffraction (XRD) analysis. The deconvolution of the Fe2p spectrum has both the satellite peaks of $Fe2p_{1/2}$ and $Fe2p_{3/2}$ at 733.92eV and 719.36eV binding energies [61]. Fe^{3+} and Fe^{2+} oxidation peaks are also observed within the deconvoluted peak of $Fe2p_{3/2}$ [61]

In the Mn2p spectrum (Fig. 8d) of the FeMn@Go sample, there are 2 peaks of $Mn2p_{1/2}$ and $Mn2p_{3/2}$ at 654.83eV and 643.73eV, respectively. The ΔeV of these peaks is 11.1 eV, which indicates the presence of Mn_2O_3 [63]. This concurs with the findings of XRD analysis.

The C1s spectrum (Fig. 9a) obtained for the FeMnNa@GO catalyst reveals a complex spectral pattern due to the presence of graphene oxide and its interaction with Fe. Splitting of the C–C bonding peak into sp3 and sp2 hybridization states was observed, with an energy difference of 0.9 eV. The sp^3 hybridization peak is at 284.87 eV, while the sp^2 hybridization peak is at 283.97 eV [1]. This confirms the presence of graphene oxide and is consistent with the TEM images. There was a C–*O*–C peak at 286.19eV and a C–O peak at 287.49ev. A shake-up peak is also visible around 290.58 eV due to the interaction of π-π· [59].

In the O1s spectrum (Fig. 9b) of the catalyst FeMnNa@GO, the peaks of Organic C–O, Organic C¯–O, and Metal oxides are observed at 531.06 eV, 532.93 eV, 529.50 eV, respectively [60]. A Na auger peak is visible in the O1s spectrum at 535.80eV, which proves the existence of Na in the catalyst [60].

The Fe2p spectrum (Fig. 9c) of the FeMnNa@GO catalyst confirms the formation of Fe_3O_4, which is consistent with the XRD results. The deconvolution of the Fe2p spectrum has both the satellite peaks of $Fe2p_{1/2}$ and $Fe2p_{3/2}$ at 733.33eV and 719.51eV binding energies [61]. The Fe^{3+} oxidation peak is at 728.74eV, and the Fe^{2+} oxidation peak is at 725.01eV within the deconvoluted peak of $Fe2p_{1/2}$. There is a Fe $^{3+}$ oxidation peak at 715.68eV and Fe^{2+} oxidation peaks at 710.88eV and 712.35eV within the deconvoluted peak of $Fe2p_{3/2}$ [61] There is a charge shift of ~+1eV in the Fe2p spectrum of the FeMnNa@GO catalyst compared to that of the FeMn@GO catalyst [63].

In the Mn2p spectrum (Fig. 9d) of the FeMnNa@Go sample, there are 2 peaks of $Mn2p_{1/2}$ and $Mn2p_{3/2}$ at 654.54eV and 643.04eV, respectively. The ΔeV of these peaks is 11.5eV, which denotes the presence of Mn_2O_3 [63,64]. This was confirmed from the findings of the XRD analysis.

3. Results and discussion

3.1. Catalytic activity studies

To determine the optimal temperature for the selectivity and CO conversion, the reaction temperature was increased from 200 to 350 °C with a molar ratio of H_2: CO (2:1), using 20 bar pressure and 12000 GHSV. The flow rate of the N_2 gas was kept steady at 1.5 ml/min [65]. CO conversion and selectivity were determined using the following equations [66,67]:

$$X_{CO}\% = \frac{F_{CO,in} - F_{CO,out}}{F_{CO,in}} \times 100 \quad (1)$$

$$CH_4 Selectivity\ (\%) = \frac{mCH_4}{mCH_4 + 2mC_2H_6 + 3mC_3H_8 + 3mC_3H_6 + 4mC_4H_{10}} \times 100 \quad (2)$$

$$C_2H_6 Selectivity\ (\%) = \frac{2mC_2H_6}{mCH_4 + 2mC_2H_6 + 3mC_3H_8 + 3mC_3H_6 + 4mC_4H_{10}} \times 100 \quad (3)$$

$$C_3H_8 Selectivity\ (\%) = \frac{3mC_3H_8}{mCH_4 + 2mC_2H_6 + 3mC_3H_8 + 3mC_3H_6 + 4mC_4H_{10}} \times 100 \quad (4)$$

$$C_4H_{10} Selectivity\ (\%) = \frac{4mC_4H_{10}}{mCH_4 + 2mC_2H_6 + 3mC_3H_8 + 3mC_3H_6 + 4mC_4H_{10}} \times 100 \quad (5)$$

$$C_3H_6 Selectivity\ (\%) = \frac{3mC_3H_6}{mCH_4 + 2mC_2H_6 + 3mC_3H_8 + 3mC_3H_6 + 4mC_4H_{10}} \times 100 \quad (6)$$

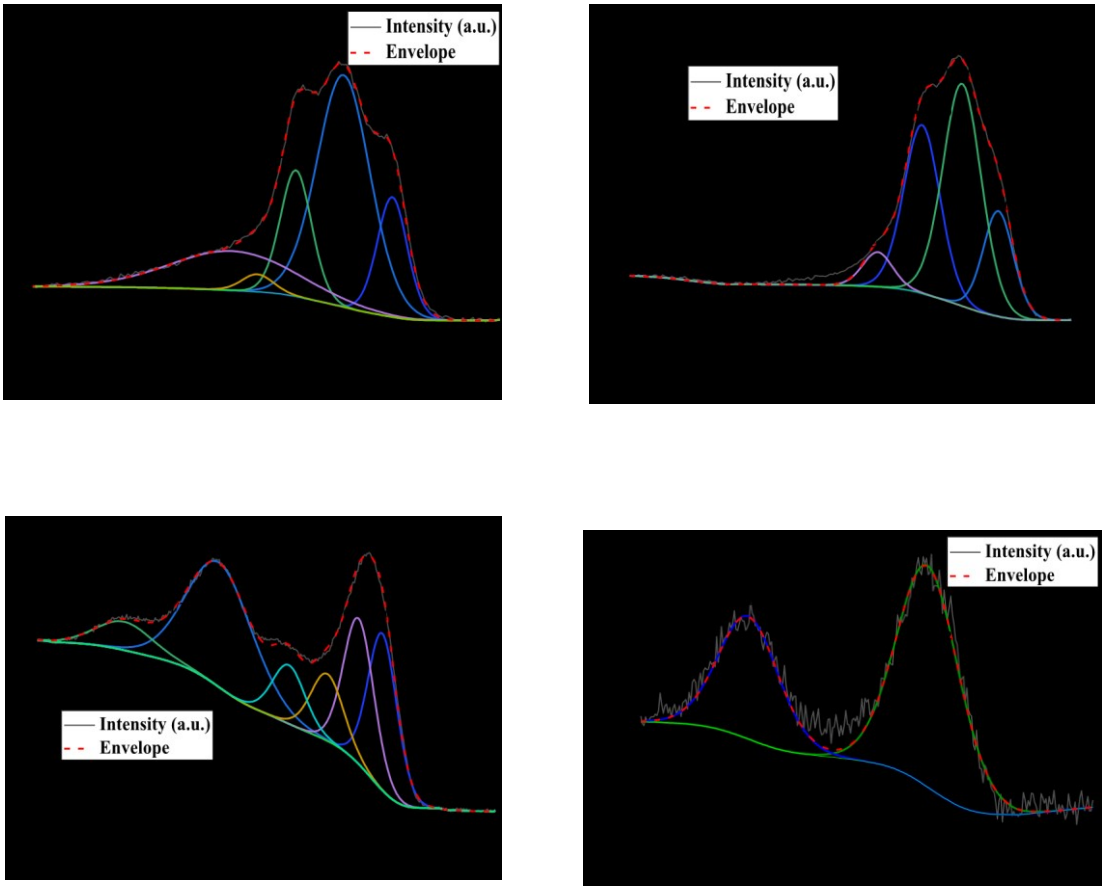

Fig. 8. XPS analyses of (a) C1s; (b) O1s; (c) Fe2p; (d) Mn2p for FeMn@GO catalyst.

As illustrated in Fig. 10a, for the Fe@GO catalyst, CO conversion increased above 290 °C. As the temperature changed, the CO conversion improved at a rate of approximately 40% per 60 °C, with approximately 80% CO conversion at 350 °C. The product selectivity of FT synthesis using the Fe@GO catalyst is also shown above. Propene is a desired product, and at 290 °C, propene was the most prevalent product and comprised about 16% of the products, with CO_2 having a large share of selectivity as well. At 320 °C, the CO conversion was approximately 30% higher and the selectivity for propene was 14%. At this temperature, the selectivity towards CO_2 was around 9%, down from 14% selectivity towards CO_2 at 290 °C. Note that long-chain hydrocarbons are waxes or liquids, and are not shown in the gas product selectivity in Fig. 10 [68]. This is because the gaseous products were analyzed via GC-MS, and the waxes and liquids were caught in the hot and cold traps, respectively. It can be assumed that the selectivity not shown in the Figure consists

mainly of waxes, liquid hydrocarbons, and water vapor (the supplemental information contains the GC-MS of the liquid samples) (See Fig. S6).

Fig. 10 shows the FeMn@GO catalyst activity in terms of product selectivity and CO conversion over a wide range of reaction temperatures. The CO conversion increased significantly with rise in temperature, with a maximum CO conversion of 97% obtained with the FeMn@GO catalyst.

The propene selectivity slightly increased at higher temperatures. Conversely, in this temperature range, greater hydrocarbon selectivity was observed in comparison to the other catalysts; the C2–C4 selectivity remained almost the same as the temperature increased.

The FTS reaction is thermodynamically favored for the hydrogenation of CO_2 to form CO at higher temperatures, while the water-gas shift reaction is exothermic [61]. Fig. 10 depicts the CO conversion with temperature for FeMn@GO; the conversion was quite low, approximately 10% at 200 °C, it reaches a maximum at 350 °C. Although the CO conversion steadily increased by 15%, our findings suggests that the metal promoters in FeMn@GO played individual and important roles in syngas conversion and C_1–C_4 product distribution at 20 bar.

The CO conversion and gas product selectivity for reactions using the FeMnNa@GO catalyst are shown in Fig. 10. Compared with the unpromoted catalyst, the conversion was higher at all temperatures and began to increase at a lower temperature of 200 °C. The catalytic activity was bolstered by the promoter metals, reaching over 90% CO conversion at 350 °C. At this temperature, the propene and CO_2 selectivities were both approximately 6%.

However, propene selectivity tended to increase with temperature, whereas CO_2 selectivity reached 8% at 260 °C and then decreased with increasing temperature. This catalyst also yielded a considerable amount of liquid products, which are long-chain hydrocarbons [69]. The analysis of the liquid products from this reaction by GC-MS is shown in the supplementary data (See Fig. S6).

3.2. Time on stream studies

The FTS reaction was performed for 30 h at 320 °C under the same operating conditions (Fig. 11) to examine the time-on-stream behavior of all catalysts. Stable CO conversion (Fig. 11a) was observed: Fe@GO 65–70%, FeMn@GO 85–90%, and FeMnNa@GO 90–95% CO up to 30 h. FeMnNa@GO exhibited higher CO conversion than FeMn@GO and Fe@GO. The selectivity to lower hydrocarbons remained nearly constant during the time-on-stream study for all catalysts. The C_{4+} selectivity was quite high at the beginning and very stable for FeMnNa@GO (85–90%) and FeMn@GO (70–75%), but for Fe@GO, the selectivity slightly decreased after 20 h and then increased again to an optimum temperature after 25 h (Fig. 11b, c and d). C_2–C_4 and lighter olefin selectivities were almost constant throughout the stability studies. Fe@GO 10–15%, FeMn@GO 15–20%, and FeMnNa@GO 5–10% [70,71].

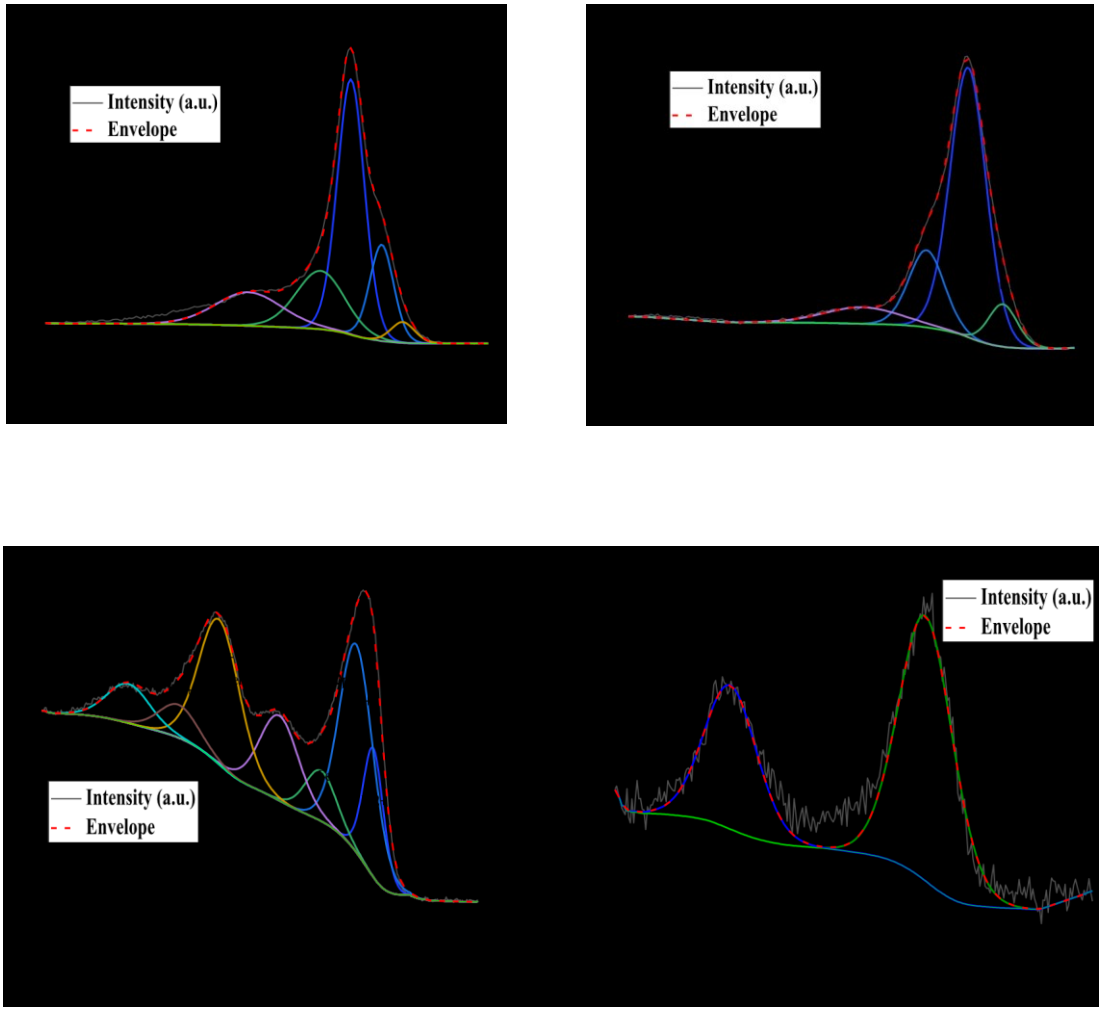

Fig. 9. XPS analysis of (a) C1s; (b) O1s; (c) Fe2p; (d) Mn2p for FeMnNa@GO catalyst.

3.3. Spent catalyst characterization

3.3.1. XRD analysis

Fig. 12 depicts the XRD patterns of all spent catalysts. After the FTS reaction, the diffraction peak corresponding to the Fe_3O_4 phase disappeared. Diffraction peaks at 2θ values of 35.45°(002), 39.45°(020), 40.72°(112), 43.43°(021), 44.19°(510), and 58.21°(222) are observed, which are attributed to the monoclinic structure of the iron carbide (Fe_5C_2) phase (JCPDS 36–1248) of the spent Fe@GO catalyst. The formation of iron carbide suggests a partial transformation of the Fe_3O_4 phase during the FTS reaction [41]. In the case of the spent FeMn@GO catalyst, the Fe_5C_2 phase was observed at the same diffraction angle as the spent Fe@GO catalyst, with an additional diffraction peak at 60.18° (113). Diffraction peaks of the Mn_2O_3 phase were noticed at 2θ values of 32.72°(222) and 68.72°(444) for the spent FeMn@GO catalyst. Iron carbide diffraction peaks were observed at 2θ values of 35.45°(002),

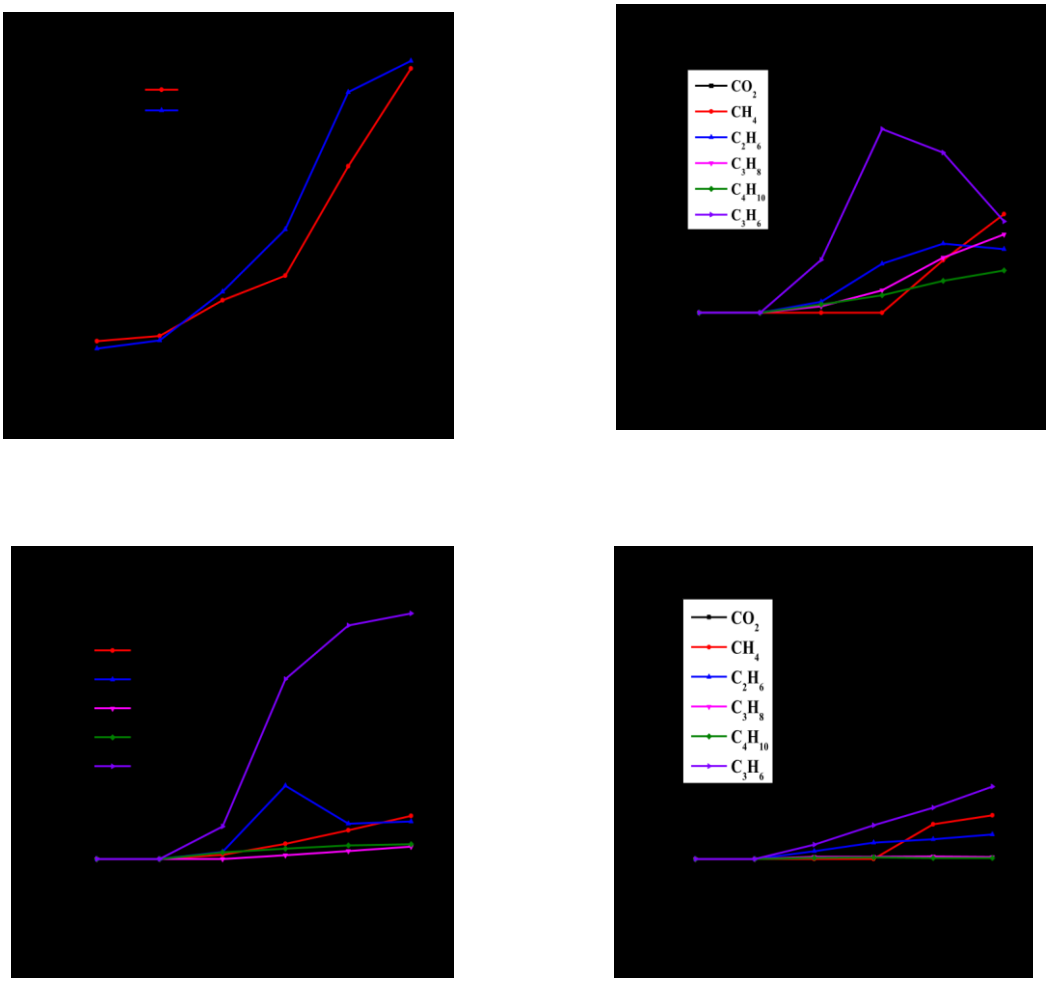

Fig. 10. Effect of temperature on CO conversion and product selectivity; (a) CO conversion of all catalysts; (b) Product selectivity of Fe@GO catalyst; (c) Product selectivity of FeMn@GO catalyst; (d) Product selectivity of FeMnNa@GO catalyst (Conditions: H_2/CO = 2, 20 bar, N_2 = 1.5 ml/min and 12000 GHSV).

41.27°(202), 60.2°(113), and 65.63°(711) for the FeMnNa@GO catalyst. The Mn_2O_3 peaks were detected at 38°(400) and 71.85°(046). The XRD profiles of all the spent catalysts are demonstrated below. The typical crystal sizes of the Fe_5C_2 and Mn_2O_3 phases were measured using the modified Scherrer equation [54]. The crystal sizes are listed in Table 5. The Fe_5C_2 crystal size of the Fe@GO catalyst was 30.66 nm. The Fe_5C_2 and Mn_2O_3 crystal sizes are 14.43 and 14.78 nm for FeMn@GO, respectively. The crystal size increased owing to the addition of Mn nanoparticles. The crystal sizes of Fe_5C_2 and Mn_2O_3 nanoparticles are 22.07 and 27.05 nm for the FeMnNa@GO catalyst. The increased crystal size of the spent catalyst may be attributed to coke deposition on the catalyst surface during the FTS reaction.

3.3.2. TGA-DSC analysis

TGA-DSC analysis was conducted on the spent catalysts after their use in the FTS reactions. Air was flowed over the spent catalysts as opposed to N_2. This is meant to burn off coke and other carbonaceous species that are now stuck to the catalyst surface as a result of the reaction. The results for the spent catalyst from TGA-DSC under airflow are shown below.

Fig. S7 depicts the TGA-DSC analysis of all spent catalysts. The spent unpromoted Fe/GO catalyst showed consistent weight loss up to 100 °C and then again at approximately 300 °C, with a region of no weight loss in between. The weight loss regions correspond to endothermic peaks in the heat flow curve, suggesting thermal degradation, whereas the region with no weight loss corresponds to an exothermic peak, suggesting crystallization at that temperature [55,56]. After this, there was a weight gain in the spent catalyst, corresponding to a sharp exothermic peak around 400 °C. This could be representative of an oxidation reaction, which is generally exothermic in nature and can cause weight gain in the sample [58]. Subsequently, the catalyst underwent thermal degradation for the remainder of the analysis up to 1000 °C.

The spent catalysts containing promoters showed a higher magnitude of weight gain in the TGA-DSC analysis, with a very fast weight gain from 200 °C to about 500 °C. These weight gain regions correspond to the slight exothermic peaks in the heat flow curves, suggesting that this weight gain is the result of oxidation reactions [58]. It is also possible that the weight gain is a result of the adsorption of air or crystallization of spent catalysts [56,72].

3.3.3. SEM analysis

Fig. S8 shows SEM images of the Fe@GO, FeMn@GO, and FeMnNa@GO spent catalysts. After the stability investigation, the surface morphology changed. Particle agglomeration was viewed for all the spent catalysts. The particle size of Fe@GO spent catalyst is 254.68 nm. The particle size of FeMn@GO and FeMnNa@GO catalysts are 491.88 and 462.83 nm respectively. As compared to fresh catalysts, the spent catalysts particle size increased due to sintering of particles during FTS process.

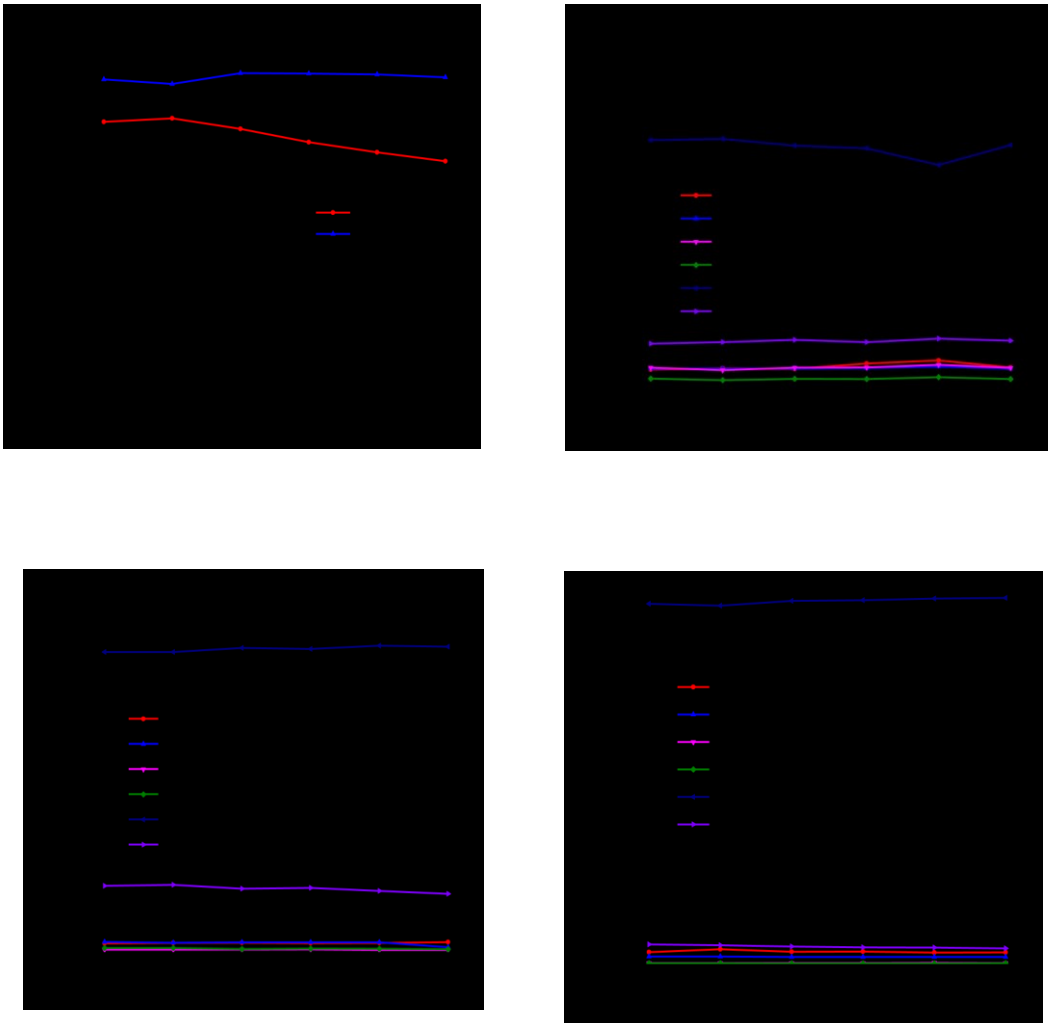

Fig. 11. Time-on-stream behavior of all catalysts (Conditions: H_2/CO = 2, 20 bar, 12000 GHSV at 320 °C for 30 h and N_2 = 1.5 ml/min).

3.3.4. Structure-property correlation of the catalysts

The activity of the iron on carbon supported catalysts is strongly dependent on the structural properties of the carbon support used. Graphene has inherent thermal and electrical conductivity. This is also important to remove the excess amount of heat during exothermic FTS process. So, the support is very stable at higher temperatures and under severe reaction conditions. The structural properties depend on metal- support interaction, the degree of graphitization of graphene support, surface area and modification of iron-carbon supported catalysts with promoters.

Metal-support interaction is the significant factor which affects the FTS process in terms of activity, selectivity, and catalyst activity. Silica, alumina, and titania supports have been used by many researchers previously for the FTS process. These supports exhibited strong metal- support interaction, which tends to reduce the catalysts at higher temperatures. Currently, researchers have taken advantage of weak interaction of carbon support with metals. The graphene oxide supported iron catalysts is easy to reduce at lower temperature. The carbon-based support enhances the formation of olefin during FTS process. It has advantages in terms of heat transfer of the reaction. The large contact surface area of graphene nanosheets increase the activity of the catalyst during FTS by providing large surface density for reactants and decreasing mass transfer limitations [73]. The carbon support is suitable for FTS process because of its thermal stability. It does not form mixed oxides, which are difficult to reduce. The metal-support interaction is affected by different factors such as preparation method and functionalization of the support with functional groups such as nitrogen and oxygen. These factors introduced defects in the support which affect the formation of iron carbide by increasing or decreasing the reduction temperature. The promoters also influenced the metal-support interaction, which leads to the formation of iron carbide during reduction. In this study, we observed the formation of iron carbide in the spent catalyst as evidenced by XRD analysis.

An important characteristic of graphene is that it can be graphitized compared to others carbon supports [74]. So, it is easy to fabricate the fibers in graphene in the same direction compared to other carbon supports. Different kinds of defects are influenced by its structure and physiochemical properties [75]. It can change the topology or curvature of graphene [75]. The chemical activity also changes due to its defects [75]. Promoters also influence the surface chemistry of graphene [76].

The performance of catalyst in FTS process is affected by particle size, structural properties, surface area and porosity [77]. The catalysts should have large surface area and pore volume to accommodate large amounts of metal loading.

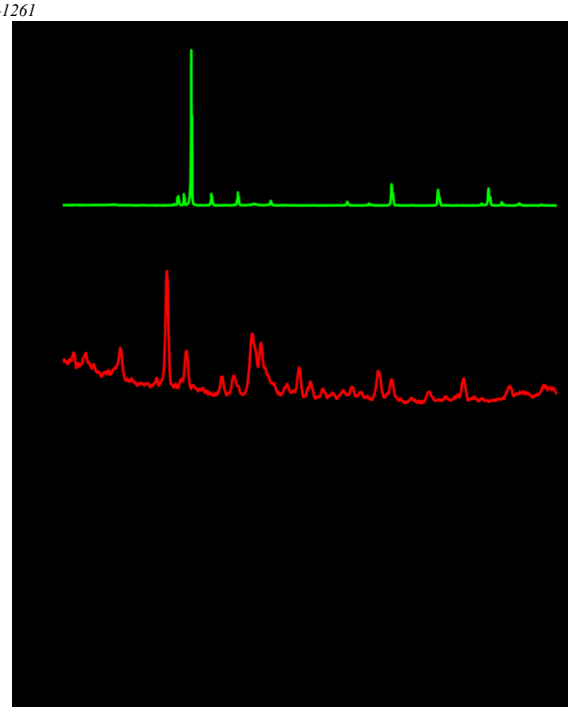

Fig. 12. XRD patterns of (a) Fe@GO; (b) FeMn@GO; (c) FeMnNa@GO spent catalysts.

Table 5
Crystal size[a] based on XRD analysis.

Spent Catalyst	Average crystal size (nm) (Fe_5C_2)	Average crystal size (nm) (Mn_2O_3)
Fe@GO	30.66	
FeMn@GO	14.43	14.78
FeMnNa@GO	22.07	27.05

[a] Using the modified Scherrer equation [54].

4. Conclusions

Catalysts were prepared in two steps. In the first step, the metal core was synthesized using a layer-by-layer method. Graphene oxide (GO) was then attached to the core part in the second stage. **The surface area and pore volume morphology of the catalyst changed after the addition of the Mn and Na promoters.** The surface area decreased slightly upon the addition of promoter metals, and the FeMn@GO sample had a lower pore volume and pore diameter compared to the unpromoted Fe@GO catalyst and FeMnNa@GO catalyst. The reduction behavior of all the catalysts was affected by the addition of Mn and Na. An understanding of the oxidation states of metals helped to reduce the catalyst within appropriate temperature range to activate the catalyst. The XRD results showed that the crystalline grain size also varied in the presence of the different promoters. The presence of the promoter metals lowered the temperatures at which the catalysts were reduced, and the FeMn@GO catalyst was reduced at the lowest temperature. The Mn- and Na-promoted catalysts exhibited enhanced catalytic activities in terms of product selectivity and CO conversion. In addition, the highest propene selectivity was obtained for the FeMn@GO catalyst with variation of the reaction temperature. The stability study revealed that all catalysts were stable for CO conversion over a 30 h reaction time. **The highest CO conversion was monitored with the FeMnNa@GO catalyst, which yielded the greatest amount of liquid product. The propene selectivity from the stability studies at 320 °C followed the order FeMn@GO > Fe@GO > FeMnNa@GO.** A stainless steel microreactor was successfully used at high pressure to screen the catalyst in terms of conversion and product selectivity for FTS reactions. Spent catalyst studies showed the formation of Fe-carbide in the spent catalysts, indicating that the graphene oxide reacted with the Fe in the catalysts when the catalyst was in its active state.

Acknowledgment

This research was conducted at the North Carolina Agricultural and Technical State University in the Applied Science Technology and Chemistry Departments. The partial financial support for this project from NSF- CREST (Award Number:1736173) and DOE-BES (Award Number: DE SC0022230) is acknowledged. Some of the analytical characterizations were carried out at the Joint School of Nanoscience and Nanoengineering and were supported by the National Science Foundation (Grant ECCS-2025462) of the National Nanotechnology Coordinated Infrastructure (NNCI) initiative. The authors gratefully acknowledge the instrumental guidance provided by Dr Richard Abrokwah. We thank Dr. Shima Masoumi for SEM and Mr. Shashwata Chakraborty for FTIR characterization of the catalysts. We also thank Dr. Shobha Mantripragada and Dr. Olubunmi Ayodele for the GC-MS studies of the liquid samples from the FT reactions.

Appendix A. Supplementary data

Supplementary data to this article can be found online at https://doi.org/10.1016/j.ijhydene.2024.03.086.

References

[1] Fischer F, Tropsch H. The synthesis of petroleum at atmospheric pressures from gasification products of coal. Brennstoff-Chemie 1926;7:97–104.
[2] Mohanty P, Pant KK, Mittal R. Hydrogen generation from biomass materials: challenges and opportunities. WIREs Energy and Environment 2015;4:139–55. https://doi.org/10.1002/wene.111.
[3] Heidenreich S, Foscolo PU. New concepts in biomass gasification. Prog Energy Combust Sci 2015;46:72–95. https://doi.org/10.1016/j.pecs.2014.06.002.
[4] Sansaniwal SK, Rosen MA, Tyagi SK. Global challenges in the sustainable development of biomass gasification: an overview. Renew Sustain Energy Rev 2017;80:23–43. https://doi.org/10.1016/j.rser.2017.05.215.
[5] Bej B, Bepari S, Pradhan NC, Neogi S. Production of hydrogen by dry reforming of ethanol over alumina supported nano-NiO/SiO2 catalyst. Catal Today 2017;291: 58–66. https://doi.org/10.1016/j.cattod.2016.12.010.
[6] Bepari S, Kuila D. Steam reforming of methanol, ethanol and glycerol over nickel- based catalysts-A review. Int J Hydrogen Energy 2020;45:18090–113. https://doi.org/10.1016/j.ijhydene.2019.08.003.
[7] Bepari S, Khan M, Li X, Mohammad N, Kuila D. Effect of Ce and Zn on Cu-based mesoporous carbon catalyst for methanol steam reforming. Top Catal 2023;66: 375–92. https://doi.org/10.1007/s11244-022-01772-6.
[8] Bepari S, Pradhan NC, Dalai AK. Selective production of hydrogen by steam reforming of glycerol over Ni/Fly ash catalyst. Catal Today 2017;291:36–46. https://doi.org/10.1016/j.cattod.2017.01.015.
[9] Bepari S, Basu S, Pradhan NC, Dalai AK. Steam reforming of ethanol over cerium-promoted Ni-Mg-Al hydrotalcite catalysts. Catal Today 2017;291:47–57. https://doi.org/10.1016/j.cattod.2017.01.027.
[10] Bepari S, Sarkar JJ, Pradhan NC. Kinetics of ethanol steam reforming over Ni/ Olivine catalyst. Int J Hydrogen Energy 2022;47:30843–60. https://doi.org/10.1016/j.ijhydene.2022.02.032.
[11] Davis BH. Fischer–Tropsch synthesis: current mechanism and futuristic needs. Fuel Process Technol 2001;71:157–66. https://doi.org/10.1016/S0378-3820(01) 00144-8.
[12] Joos L, Filot IAW, Cottenier S, Hensen EJM, Waroquier M, Van Speybroeck V, et al. Reactivity of CO on carbon-covered cobalt surfaces in Fischer–Tropsch synthesis. J Phys Chem C 2014;118:5317–27. https://doi.org/10.1021/jp4109706.
[13] Martinelli M, Gnanamani MK, LeViness S, Jacobs G, Shafer WD. An overview of Fischer-Tropsch Synthesis: XtL processes, catalysts and reactors. Appl Catal Gen 2020;608:117740. https://doi.org/10.1016/j.apcata.2020.117740.
[14] Jiao F, Bai B, Li G, Pan X, Ye Y, Qu S, et al. Disentangling the activity-selectivity trade-off in catalytic conversion of syngas to light olefins. Science 2023;380: 727–30. https://doi.org/10.1126/science.adg2491. 1979.
[15] Zhang M, Fang K, Lin M, Hou B, Zhong L, Zhu Y, et al. Controlled fabrication of iron oxide/mesoporous silica core–shell nanostructures. J Phys Chem C 2013;117: 21529–38. https://doi.org/10.1021/jp4049583.
[16] Wu K, Liang Y, Jiao N. Azidation in the difunctionalization of olefins. Molecules 2016;21:352. https://doi.org/10.3390/molecules21030352.
[17] Torres Galvis HM, Bitter JH, Khare CB, Ruitenbeek M, Dugulan AI, De Jong KP. Supported iron nanoparticles as catalysts for sustainable production of lower olefins. Science 2012;335:835–8. https://doi.org/10.1126/science.1215614. 1979. [18] Torres Galvis HM,

Bitter JH, Davidian T, Ruitenbeek M, Dugulan AI, De Jong KP. Iron particle size effects for direct production of lower olefins from synthesis gas. J Am Chem Soc 2012;134:16207–15. https://doi.org/10.1021/ja304958u.

[19] Jiao F, Li J, Pan X, Xiao J, Li H, Ma H, et al. Selective conversion of syngas to light olefins. Science 2016;351:1065–8. https://doi.org/10.1126/science.aaf1835. 1979.

[20] Abello S, Montan´ e D. Exploring iron-based multifunctional catalysts for fischer- ´ tropsch synthesis: a review. ChemSusChem 2011;4:1538–56. https://doi.org/ 10.1002/cssc.201100189.

[21] Santos VP, Wezendonk TA, Ja´en JJD, Dugulan AI, Nasalevich MA, Islam H-U, et al. Metal organic framework-mediated synthesis of highly active and stable Fischer- Tropsch catalysts. Nat Commun 2015;6:6451. https://doi.org/10.1038/ ncomms7451.

[22] Zhao H, Zhu Q, Gao Y, Zhai P, Ma D. Iron oxide nanoparticles supported on pyrolytic graphene oxide as model catalysts for Fischer Tropsch synthesis. Appl Catal Gen 2013;456:233–9. https://doi.org/10.1016/j.apcata.2013.03.006.

[23] Wei Y, Zhang C, Liu X, Wang Y, Chang Q, Qing M, et al. Enhanced Fischer–Tropsch performances of graphene oxide-supported iron catalysts *via* argon pretreatment. Catal Sci Technol 2018;8:1113–25. https://doi.org/10.1039/C7CY02449E.

[24] Cheng Y, Lin J, Xu K, Wang H, Yao X, Pei Y, et al. Fischer–tropsch synthesis to lower olefins over potassium-promoted reduced graphene oxide supported iron catalysts. ACS Catal 2016;6:389–99. https://doi.org/10.1021/acscatal.5b02024.

[25] Moussa SO, Panchakarla LS, Ho MQ, El-Shall MS. Graphene-supported, iron-based nanoparticles for catalytic production of liquid hydrocarbons from synthesis gas: the role of the graphene support in comparison with carbon nanotubes. ACS Catal 2014;4:535–45. https://doi.org/10.1021/CS4010198/SUPPL_FILE/CS4010198_SI_ 001.PDF.

[26] Cheng Y, Lin J, Xu K, Wang H, Yao X, Pei Y, et al. Fischer-tropsch synthesis to lower olefins over potassium-promoted reduced graphene oxide supported iron catalysts. ACS Catal 2016;6:389–99. https://doi.org/10.1021/ACSCATAL.5B02024/SUPPL_ FILE/CS5B02024_SI_001.PDF.

[27] Wei Y, Yan L, Ma C, Zhang C, Sun S, Wen X, et al. Mesoporous iron oxide nanoparticle-decorated graphene oxide catalysts for fischer-tropsch synthesis. ACS Appl Nano Mater 2020;3:7182–91. https://doi.org/10.1021/ACSANM.0C01522/ SUPPL_FILE/AN0C01522_SI_001.PDF.

[28] Wei Y, Luo D, Yan L, Liu J, Cheng Q, Cai M, et al. Glucose-induced monodisperse iron oxide/graphene oxide catalysts for efficient fischer-tropsch synthesis. Energy Fuel 2021;35:4428–36. https://doi.org/10.1021/ACS.ENERGYFUELS.1C00168/ SUPPL_FILE/EF1C00168_SI_001.PDF.

[29] Cheng Y, Lin J, Wu T, Wang H, Xie S, Pei Y, et al. Mg and K dual-decorated Fe-on- reduced graphene oxide for selective catalyzing CO hydrogenation to light olefins with mitigated CO2 emission and enhanced activity. Appl Catal, B 2017;204: 475–85. https://doi.org/10.1016/J.APCATB.2016.11.058.

[30] Taghavi S, Tavasoli A, Asghari A, Signoretto M. Loading and promoter effects on the performance of nitrogen functionalized graphene nanosheets supported cobalt Fischer-Tropsch synthesis catalysts. Int J Hydrogen Energy 2019;44:10604–15. https://doi.org/10.1016/J.IJHYDENE.2019.03.015.

[31] He K, Chen G, Zeng G, Chen A, Huang Z, Shi J, et al. Three-dimensional graphene supported catalysts for organic dyes degradation. Appl Catal, B 2018;228:19–28. https://doi.org/10.1016/J.APCATB.2018.01.061.

[32] MacHado BF, Serp P. Graphene -based materials for catalysis. Catal Sci Technol 2011;2:54–75. https://doi.org/10.1039/C1CY00361E.

[33] Guo L, Guo Z, Liang J, Yong X, Sun S, Zhang W, et al. Quick microwave assembling nitrogen-regulated graphene supported iron nanoparticles for Fischer-Tropsch synthesis. Chem Eng J 2022;429:132063. https://doi.org/10.1016/J. CEJ.2021.132063.

[34] Sun B, Yu G, Lin J, Xu K, Pei Y, Yan S, et al. A highly selective Raney Fe@HZSM-5 Fischer–Tropsch synthesis catalyst for gasoline production: one-pot synthesis and unexpected effect of zeolites. Catal Sci Technol 2012;2:1625. https://doi.org/ 10.1039/c2cy20155k.

[35] Su L, Jing Y, Zhou Z. Li ion battery materials with core–shell nanostructures. Nanoscale 2011;3:3967. https://doi.org/10.1039/c1nr10550g.

[36] Jacobs G, Ma W, Davis B. Influence of reduction promoters on stability of cobalt/g-alumina fischer-tropsch synthesis catalysts. Catalysts 2014;4:49–76. https://doi. org/10.3390/catal4010049.

[37] Anderson RB, Friedel RA, Storch HH. Fischer-tropsch reaction mechanism involving stepwise growth of carbon chain. J Chem Phys 1951;19:313–9. https:// doi.org/10.1063/1.1748201.

[38] Chen Y, Xu Y, Cheng DG, Chen Y, Chen F, Lu X, et al. Synthesis of CuO-ZnO- Al2O3@ SAPO-34 core@shell structured catalyst by intermediate layer method. Pure Appl Chem 2014;86:775–83. https://doi.org/10.1515/pac-2013-1121. IUPAC Secretariat.

[39] Zhao H, Zhu Q, Gao Y, Zhai P, Ma D. Iron oxide nanoparticles supported on pyrolytic graphene oxide as model catalysts for Fischer Tropsch synthesis. Appl Catal Gen 2013;456:233–9. https://doi.org/10.1016/j.apcata.2013.03.006.

[40] Alvand M, Shemirani F. Fabrication of Fe3O4@graphene oxide core-shell nanospheres for ferrofluid-based dispersive solid phase extraction as exemplified for Cd(II) as a model analyte. Microchim Acta 2016;183:1749–57. https://doi.org/ 10.1007/s00604-016-1805-8.

[41] Xu Y, Wang J, Ma G, Bai J, Du Y, Ding M. Selective conversion of syngas to olefins- rich liquid fuels over core-shell FeMn@SiO2 catalysts. Fuel 2020;275:117884. https://doi.org/10.1016/j.fuel.2020.117884.

[42] Viswanadham N, Kamble R, Singh M, Kumar M, Murali Dhar G. Catalytic properties of nano-sized ZSM-5 aggregates. Catal Today 2009;141:182–6. https:// doi.org/10.1016/j.cattod.2008.03.026.

[43] Tao Z, Yang Y, Wan H, Li T, An X, Xiang H, et al. Effect of manganese on a potassium-promoted iron-based Fischer-Tropsch synthesis catalyst. Catal Lett 2007;114:161–8. https://doi.org/10.1007/s10562-007-9060-6.

[44] Duran FG, Barbero BP, Cadús LE, Rojas C, Centeno MA, Odriozola JA. Manganese ´ and iron oxides as combustion catalysts of volatile organic compounds. Appl Catal, B 2009;92:194–201. https://doi.org/10.1016/j.apcatb.2009.07.010.

[45] Mu J, Chen B, Guo Z, Zhang M, Zhang Z, Zhang P, et al. Highly dispersed Fe3O4 nanosheets on one-dimensional carbon nanofibers: synthesis, formation mechanism, and electrochemical performance as supercapacitor electrode materials. Nanoscale 2011;3:5034. https://doi.org/10.1039/c1nr10972c.

[46] Li Y, Yang P, Jiang F, Liu B, Xu Y, Liu X. Effect of potassium on GO-modified large Fe3O4 microspheres for the production of α-olefins. J Fuel Chem Technol 2021;49: 933–44. https://doi.org/10.1016/S1872-5813(21)60063-4.

[47] Lu J, Yang L, Xu B, Wu Q, Zhang D, Yuan S, et al. Promotion effects of nitrogen doping into carbon nanotubes on supported iron fischer–tropsch catalysts for lower olefins. ACS Catal 2014;4:613–21. https://doi.org/10.1021/cs400931z.

[48] Abbaslou RMM, Tavassoli A, Soltan J, Dalai AK. Iron catalysts supported on carbon nanotubes for Fischer–Tropsch synthesis: effect of catalytic site position. Appl Catal Gen 2009;367:47–52. https://doi.org/10.1016/j.apcata.2009.07.025.

[49] Herranz T, Rojas S, Ojeda M, Perez-Alonso FJ, Terreros P, Pirota K, et al. Synthesis, ´ structural features, and reactivity of Fe− Mn mixed oxides prepared by microemulsion. Chem Mater 2006;18:2364–75. https://doi.org/10.1021/ cm052568i.

[50] Zhang Z, Dai W, Xu X, Zhang J, Shi B, Xu J, et al. MnO_x promotional effects on olefins synthesis directly from syngas over bimetallic Fe-MnO_x/SiO_2 catalysts. AIChE J 2017;63:4451–64. https://doi.org/10.1002/aic.15796.

[51] Li J-B, Ma H-F, Zhang H-T, Sun Q-W, Ying W-Y, Fang D-Y. Sodium promoter on iron-based catalyst for direct catalytic synthesis of light alkenes from syngas. Fuel Process Technol 2014;125:119–24. https://doi.org/10.1016/j. fuproc.2014.03.017.

[52] Ribeiro MC, Jacobs G, Pendyala R, Davis BH, Cronauer DC, Kropf AJ, et al. Fischer–Tropsch synthesis: influence of Mn on the carburization rates and activities of Fe-based catalysts by TPR-EXAFS/XANES and catalyst testing. J Phys Chem C 2011;115:4783–92. https://doi.org/10.1021/jp111728h.

[53] Wang D, Zhou X, Ji J, Duan X, Qian G, Zhou X, et al. Modified carbon nanotubes by $KMnO_4$ supported iron Fischer–Tropsch catalyst for the direct conversion of syngas to lower olefins. J Mater Chem A Mater 2015;3:4560–7. https://doi.org/10.1039/ C4TA05202A.

[54] Monshi A, Foroughi MR, Monshi MR. Modified scherrer equation to estimate more accurately nano-crystallite size using XRD. World J Nano Sci Eng 2012;2:154–60. https://doi.org/10.4236/wjnse.2012.23020.

[55] Implementation of DSC analysis in reaction kinetics during heating of Ti-50...: EBSCOhost. n.d. https://web-p-ebscohost-com.ncat.idm.oclc.org/ehost/pdf viewer/pdfviewer?vid=1&sid=4b18f546-f843-4bfc-8d3a-4493b4cff3b2%40redis. [Accessed 11 March 2023].

[56] Zemenova P, Kr´ al R, Nitsch K, Kní´ ˇzek K, Cihla´ˇr A, Bystˇrický A. Characterization and crystallization kinetics of Er-doped Li2O–Y2O3–P2O5 glass studied by non- isothermal DSC analysis. J Therm Anal Calorim 2016;125:1431–7. https://doi.org/ 10.1007/S10973-016-5730-1.

[57] Abbasi M, Mirzaei AA, Atashi H. Hydrothermal synthesis of Fe-Ni-Ce nano- structure catalyst for Fischer-Tropsch synthesis: characterization and catalytic performance. 2019. https://doi.org/10.1016/j.jallcom.2019.05.314.

[58] Thermal oxidative stability analysis of hoki and tuna oils by Differential ...: EBSCOhost. n.d, https://web-s-ebscohost-com.ncat.idm.oclc.org/ehost/pdfviewer/ pdfviewer?vid=1&sid=95d4c5e7-e8e1-443e-bc25-07c2631f8517%40redis. [Accessed 11 March 2023].

[59] Shchukarev AV, Korolkov DV. XPS Study of group IA carbonates. Open Chem 2004; 2:347–62. https://doi.org/10.2478/BF02475578.

[60] Nohira H, Tsai W, Besling W, Young E, Petry J, Conard T, et al. Characterization of ALCVD-Al2O3 and ZrO2 layer using X-ray photoelectron spectroscopy. J Non-Cryst Solids 2002;303:83–7. https://doi.org/10.1016/S0022-3093(02)00970-5.

[61] Amin MO, D'Cruz B, Madkour M, Al-Hetlani E. Magnetic nanocomposite-based SELDI probe for extraction and detection of drugs, amino acids and fatty acids. Microchim Acta 2019;186:1–10. https://doi.org/10.1007/S00604-019-3623-2/ FIGURES/6.

[62] Uhlig I, Szargan R, Nesbitt HW, Laajalehto K. Surface states and reactivity of pyrite and marcasite. Appl Surf Sci 2001;179:222–9. https://doi.org/10.1016/S0169-4332(01)00283-5.

[63] Biesinger MC, Payne BP, Grosvenor AP, Lau LWM, Gerson AR, Smart RSC. Resolving surface chemical states in XPS analysis of first row transition metals, oxides and hydroxides: Cr, Mn, Fe, Co and Ni. Appl Surf Sci 2011;257:2717–30. https://doi.org/10.1016/J.APSUSC.2010.10.051.

[64] Ramos Sn do C, Xavier ALP, Teodoro FS, Elias MMC, Gonçalves FJ, Gil LF, et al. Modeling mono- and multi-component adsorption of cobalt(II), copper(II), and nickel(II) metal ions from aqueous solution onto a new carboxylated sugarcane bagasse. Part I: batch adsorption study. Ind Crops Prod 2015;74:357–71. https:// doi.org/10.1016/j.indcrop.2015.05.022.

[65] Arslan M, Bepari S, Abrokwah R, Mohammad N, Shajahan J, Kuila D. Effect of Al2O3 support on Co-based SiO2 core–shell catalysts for fischer–tropsch synthesis in 3D printed SS microchannel microreactor. Top Catal 2023;66:477–97. https:// doi.org/10.1007/s11244-022-01733-z.

[66] Pejova B, Isahi A, Najdoski M, Grozdanov I. Fabrication and characterization of nanocrystalline cobalt oxide thin films. Mater Res Bull 2001;36:161–70. https:// doi.org/10.1016/S0025-5408(00)00479-7.

[67] He T, Chen D, Jiao X. Controlled synthesis of Co_3O_4 nanoparticles through oriented aggregation. Chem Mater 2004;16:737–43. https://doi.org/10.1021/ cm0303033.

[68] Mohammad N, Basha OM, Bepari S, Abrokwah RY, Deshmane V, Wang L, et al. Fischer-tropsch synthesis in silicon and 3D printed stainless steel microchannel microreactors. Catalysis for clean energy and environmental sustainability. Cham: Springer International Publishing; 2021. p. 429–57. https://doi.org/10.1007/978- 3-030-65021-6_14.

[69] Bae J-S, Hong SY, Park JC, Rhim GB, Youn MH, Jeong H, et al. Eco-friendly prepared iron-ore-based catalysts for Fischer-Tropsch synthesis. Appl Catal, B 2019;244:576–82. https://doi.org/10.1016/j.apcatb.2018.11.082.

[70] Kordouli E, Pawelec B, Kordulis C, Lycourghiotis A, Fierro JLG. Hydrodeoxygenation of phenol on bifunctional Ni-based catalysts: effects of Mo promotion and support. Appl Catal, B 2018;238:147–60. https://doi.org/10.1016/ j.apcatb.2018.07.012.

[71] Bepari S, Li X, Abrokwah R, Mohammad N, Arslan M, Kuila D. Co-Ru catalysts with different composite oxide supports for Fischer–Tropsch studies in 3D-printed stainless steel microreactors. Appl Catal Gen 2020;608:117838. https://doi.org/ 10.1016/j.apcata.2020.117838.

[72] Nhandeyara S, Ramos C, Luísa A, Xavier P, Simoes Teodoro F, Madonyk M, et al. ˜ Modeling mono-and multi-component adsorption of cobalt(II), copper(II), and nickel(II) metal ions from aqueous solution onto a new carboxylated sugarcane bagasse. Part I: batch adsorption study. Ind Crops Prod 2015;74:357–71. https:// doi.org/10.1016/j.indcrop.2015.05.022.

[73] Karimi S, Tavasoli A, Mortazavi Y, Karimi A. Cobalt supported on Graphene – a promising novel Fischer–Tropsch synthesis catalyst. Appl Catal Gen 2015;499: 188–96. https://doi.org/10.1016/J.APCATA.2015.04.024.

[74] Lee HK, Lee JH, Seo JH, Chun DH, Kang SW, Lee DW, et al. Extremely productive iron-carbide nanoparticles on graphene flakes for CO hydrogenation reactions under harsh conditions. J Catal 2019;378:289–97. https://doi.org/10.1016/J. JCAT.2019.09.004.

[75] Terrones M, Botello-Mendez AR, Campos-Delgado J, L´ opez-Urías F, Vega-Cantú YI, ´ Rodríguez-Macías FJ, et al. Graphene and graphite nanoribbons: morphology, properties, synthesis, defects and applications. Nano Today 2010;5:351–72. https://doi.org/10.1016/J.NANTOD.2010.06.010.

[76] Cheng Y, Tian J, Lin J, Wang S, Xie S, Pei Y, et al. Potassium-promoted magnesium ferrite on 3D porous graphene as highly efficient catalyst for CO hydrogenation to lower olefins. J Catal 2019;374:24–35. https://doi.org/10.1016/J. JCAT.2019.04.024.

[77] Oubagaranadin JUK, Murthy ZVP. Activated carbons: classifications, properties and applications. Activated carbon: classifications, properties and applications. USA: Nova Science Publishers Inc; 2011. p. 239–66.